Preprint Title	Atmospheric Water Harvesting using functionalized Carbon Nanocones
Authors	Fernanda R. Leivas and Marcia C. Barbosa
Publication Date	28 Jul 2022
Article Type	Full Research Paper
ORCID® iDs	Marcia C. Barbosa - https://orcid.org/0000-0001-5663-6102

Atmospheric Water Harvesting using functionalized Carbon Nanocones

Fernanda R. Leivas*[1] and Marcia C. Barbosa[2]

Address: [1]Instituto de Física, Universidade Federal do Rio Grande do Sul CP 15051, 91501-970 Porto Alegre RS, Brazil and [2]Instituto de Física, Universidade Federal do Rio Grande do Sul CP 15051, 91501-970 Porto Alegre RS, Brazil

Email: Fernanda R. Leivas - fernanda.leivas@ufrgs.br

* Corresponding author

Abstract

In this work we propose using molecular dynamic simulations a method to harvest liquid water from vapor using carbon nanocones. The condensation occurs due to the presence of hydrophilic sites at the nanocone entrance. The functionalization together with the high mobility of water inside nanostructures leads to fast water flow through the nanostructure. We show that this device is able to collect water if the surface fuctionalization is properly selected.

Keywords

Atmospheric water harvesting; Nanocones; Hydrophobicity. Hydrophilicity; Nanotechnology

Introduction

Despite water being abundant in earth, there are at least four billion people suffering with water scarcity [1]. The lack of potable water results from a number of factors such as mono-culture, increasing deforestation and a growing population. [2-5].

In order to circumvent the problem of lack of fresh water scientists are developing alternative processes such as filtration of contaminated water [6], desalinization [7] and collecting water from atmosphere [8]. The atmospheric water harvesting (AWH) is a interesting option to obtain fresh water, particularly in arid and semi-arid areas, where other sources of water are inaccessible and population have long been suffering with water scarcity [9]. There are different processes to develop an AWM, from the condensation and collection of moisture; cooling the air ambient below its dew point [10,11]; using chemical and physical process in the absorption/adsorption mechanism [9,12,13]. Many of these mechanisms are inspired by structures found in nature (biomimic designs), that uses hierarchical nano/microstructures to collect water, like the *Trifolium pratense* plant the *Cotula fallax* cactus and the the *Uloborus walckenaerius* spider [14-16].

One mechanism developed by nature to capture liquid water from water vapor is present in the Namibian desert beetle, which collects water from morning steam in the desert [17]. The beetle has hydrophilic spots on its back which transform vapor into liquid water. For the collection to be efficient, below the hydrophilic spots, its wings are hydrophobic and collect the captured water from hydrophilic to hydrophilic parts by gravity. The efficiency of this process led to the development of mimetic strategies [18-21] which use the combination of wetting and dewetting properties employed by the beetle. The hydrophobic region as in the case of the Lotus is fundamental for the mobility of water.

Water also presents other anomalous behavior in addition to the hydrophobicity described above. The density and diffusion coefficient increase as the density is increased was observed in experiments and simulations in bulk water [22-24]. Water presents both super flow and slowing down when confined in biological structures with the presence of hydrophobic and hydrophilic sites [25]. Water confined in hydrophobic structures as carbon nanotubes with diameter below 2nm exhibits a fast flow that exceed values provided by classical hydrodynamics [26]. This super flow is observed because water are pushed away from the hydrophobic surface forming a single line of molecules which moves in a stressless matter.

The water superflow in nanostructures has been explored in processes of separating water from salt or in separating it from other contaminants. This high mobility of water under nanoconfinement requires huge pressures and consequently high energies [27,28]. In order to help the water entrance, and decrease the amount of required pressure, nanotubes are functionalized with hydrophilic groups [29,30]. The addition of hydrophilic regions in small diameter, however, decreases the velocity of the water molecules [31].

The high flow of water in nano structures is also useful for capturing water from the atmosphere. Nanotubes with hydrophilic sites, to capture water from atmosphere, and hydrophobic regions, to move the molecules to reservoirs [32,33] has been analyzed. Regardless presenting reasonable results regarding the capacity of capturing water, the small diameter of the nanotube entrance requires high pressures for the water to enter, what makes the process energetically costly.

One geometry which combines large surface for capturing water, and a small radius for making the molecules to flow fast, is the nanocone. Carbon nanocones (or nanohorns) are conical structures that are made predominantly of carbon, typically $2 - 5$nm in diameter and $40 - 50$nm in length. They occur on the surface of natural graphite, void CNCs can be produced for example by decomposing hydrocarbons with a plasma torch [34], and other simple techniques of production [35] and reduction [36] are also being recently developed. The CNCs are completely hydrophobic, but functionalization could be done to make some parts hydrophilic maintaining the other part hydrophobic.

Therefore the study of the behavior of water inside nanocones is relevant due to structural advantages at nanoscale [37,38]. The flow of water in nanocones is higher than the mobility observed in nanotubes [39,40]. In the presence of ions, water flow through a charged nanocone under an electrical field [41,42] , and this flow is higher than the induced by pressure. Consequently the desalination performance observed in these carbon nanocones is better than the observed in nanotubes or nanometric monolayers as graphene and MoS_2 [43,44]. Another advantage of the cone format, is the possibility of capturing more water at the larger diameter entrance, without loosing the high flow at the reduced diameter at the other parts of the cone.

Inspired by the beetle described above and the recent advantages found on the conical structure, for water harvesting, the introduction of hydrophilic groups at the nanocone entrance favors the condensation of water, while the hydrophobic sites at the smaller side of the cone generates a fast flow. This combination of nanotube shape and functionalization is key for making a device able to capture water.

In this work we investigate the process of capturing and collecting water by a functionalized carbon nanocone using molecular dynamic simulations. This process is analyzed for a system in which the larger diameter of the cone is in contact with a vapor reservoir, and the smaller diameter is in contact with an initially empty reservoir. As in the case of the Namibian beetle, the nanocone has hydrophibic and hydrophobic regions which combined generate the fast flow without the need of imposing pressure to the system. The remaining of the paper goes as follows. In the chapter two the model is presented and the simulation method explained. In chapter 3 the results as shown and discussed. Chapter 4 brings the conclusions.

Model and Simulation Details

The system is illustrated in Figure 1. It is composed by a conical carbon nanochannel between two slabs with length of $50\AA$. One slab is made of hydrophilic (green) atoms and the other slab is made of hydrophobic (carbon, gray) atoms. Both slabs are coupled to a reservoir. The hydrophobic slab is connected to a water vapor reservoir, while the hydrophiblic slab is connected initially to a vacuum reservoir. All the slabs are maintained rigid during the simulation.

The system shown in Figure 1 is made of a reservoir of size $50 * 54 * 50\AA^3$. This reservoir has two regions: a liquid water region, on the left, and a vapor water region, on the right. The number of water molecules on this simulation is 1473. The density of the vapor system is $0.38 g/cm^3$. As the simulation is conducted on NVT ensemble, pressure is variable.

The condensation is produced by a combination thermostats as illustrate in Figure 2, where the liquid region is illustrated in red while the vapor region is shown in blue. The red region does not have fixed thermostat, but the temperature varies from 800K to 300K in a dynamic process every 10000 temporal steps. The blue region, thermostat 2, maintains the temperature constant at 300K during all simulation. The variation of temperature in thermostat 1 is responsible for the conden-

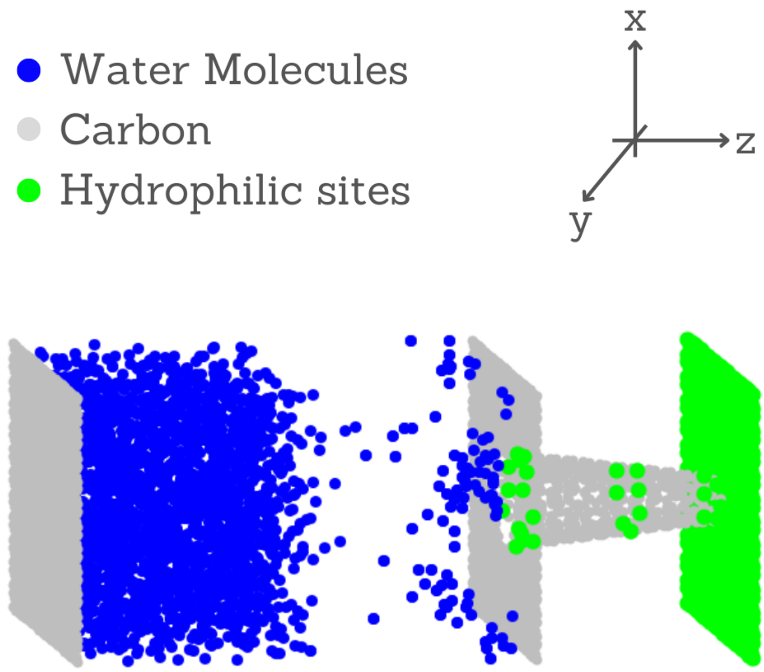

Figure 1: A Snapshot of the simulation system. A Liquid-Vapor reservoir in contact with a carbon slab and with the nanocone hydrophilic base. The nanocone tip is in contact with hydrophilic slab at a collecting reservoir.

sation at the reservoir 2. The idea of combining thermostat to produce vapor is not new, it was already employed to reproduce water evaporation and condensation [45,46].

In contact with the carbon slab on the region 1 there is a carbon nanocone (CNC), constructed by cutting the apex angle as illustrated in Figure 3. This nanocone has a length of $26\AA$, the smaller pore, the tip, has a diameter of $8.2\AA$, and the larger pore, the base, has a diameter of $17\AA$. Along the CNC there are three rings-shaped regions with hydrophilic sites; at the base, at the middle and at the tip. The hydrophilic rings are modeled as effective water-wall potentials ϵ_r. The CNC and the sheets were held fixed during the simulations, water molecules inside the nanocone are subjected to a constant temperature thermostat of $300K$.

Carbon nanocones can be produced in five different apex angles [47]. Here we use the aper-

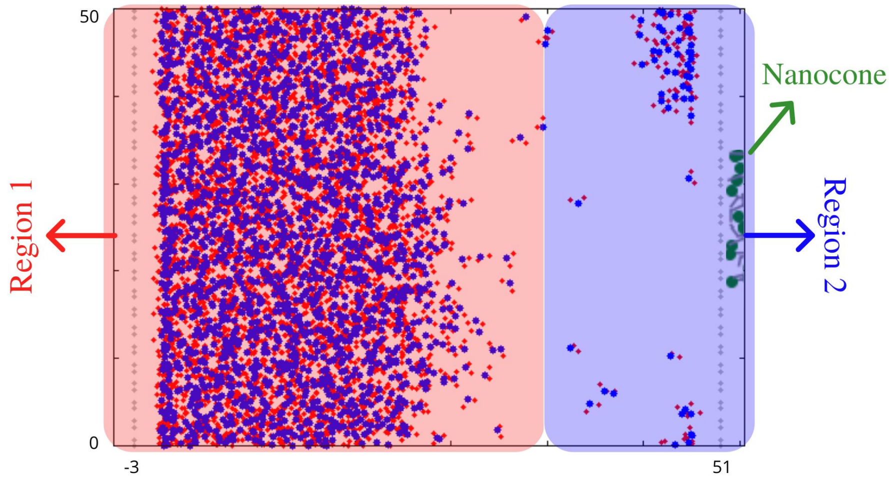

Figure 2: Part of the simulation box illustrating the two types of thermal control used in simulation. The red region represents the region 1, with temperature dynamically changing between 800k and 300k, and tregion 2 with the temperature fixed at 300k.

ture of 19.2°since it is the easier to produce in large scale [48], and because it is the nanocone which achieves the higher values of water flux when compared with the others apex angles. It also presents a lower energy barrier when compared with carbon nanotubes (CNT) [39].

The smaller size of the nanocone ends in a hydrophilic surface, which has the same structure of the hydrophobic slab. This hydrophilic surface compose the collector reservoir, which has no water at the beginning of the simulation. The dimensions of this reservoir are $50 * 20 * 50A^3$. The water molecules collected by this reservoir are maintained under a thermostat with a temperature of $300K$, as the region 2 (fig. 2).

The Molecular Dynamics (MD) simulations were performed using LAMMPS [49] package in NVT ensemble with a timestep of 0.1 fs. The TIP4P/2005 [50] water model was used, since this model give a satisfactory description of the self-diffusion coefficient [51], phase diagram, vapor-liquid equilibria [52][53], vapor-pressure and critical temperature despite being a simple model [15][54]. The SHAKE algorithm was employed to keep the rigidity of water molecules. The carbon-oxygen Lennard-Jones (LJ) pair-wise non-bonded interaction, $\epsilon_{o-c} = 0.126$kcal/mol and $\sigma_{o-c} = 3.279\AA$, was calculated using the Lorentz-Berthelot mixing rules [55]. For the interaction between hydrophilic sites and water, the same σ of carbon-oxygen interaction was fixed ($\sigma_{o-hs} = \sigma_{o-c}$), but the potential well $\epsilon_{o-hs} = \epsilon_i$ was varied. The LJ cutoff distance was $12\AA$ and the long-range electro-

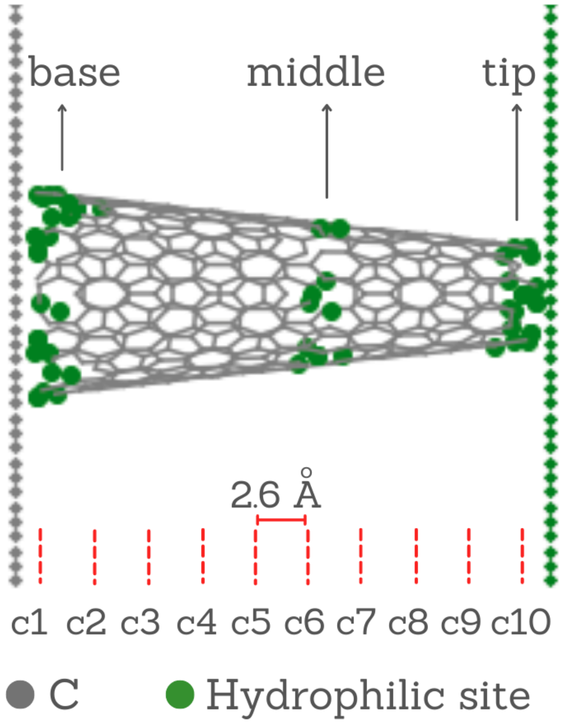

Figure 3: Carbon Nanocone (CNC) with 26$\AA$ of length, 8.2$\AA$ of diameter of the base and 17$\AA$ of diameter at the base. Hydrophilic rings are present at the base, tip and at the middle of the nanocone

static interaction were treated by the Particle Particle Mesh Method. Periodic boundary conditions was applied on the x and y directions, and non-periodic boundary conditions was applied on z direction (see Figure 1).

Results and Discussion

Figure 1 illustrates the system we analyzed composed of a water vapor reservoir in contact with the base of the nanocone. If the nanocone is fully hydrophobic no water enters into the cone. Therefore the hydrophilic rings are necessary for the water to enter an flow through the nanocone.

The water harvesting mechanism goes as follows: First, the vapor generated in region 1 from Figure 2 condenses into the slab of region 2 forming droplets. Those droplets are attracted to the hy-

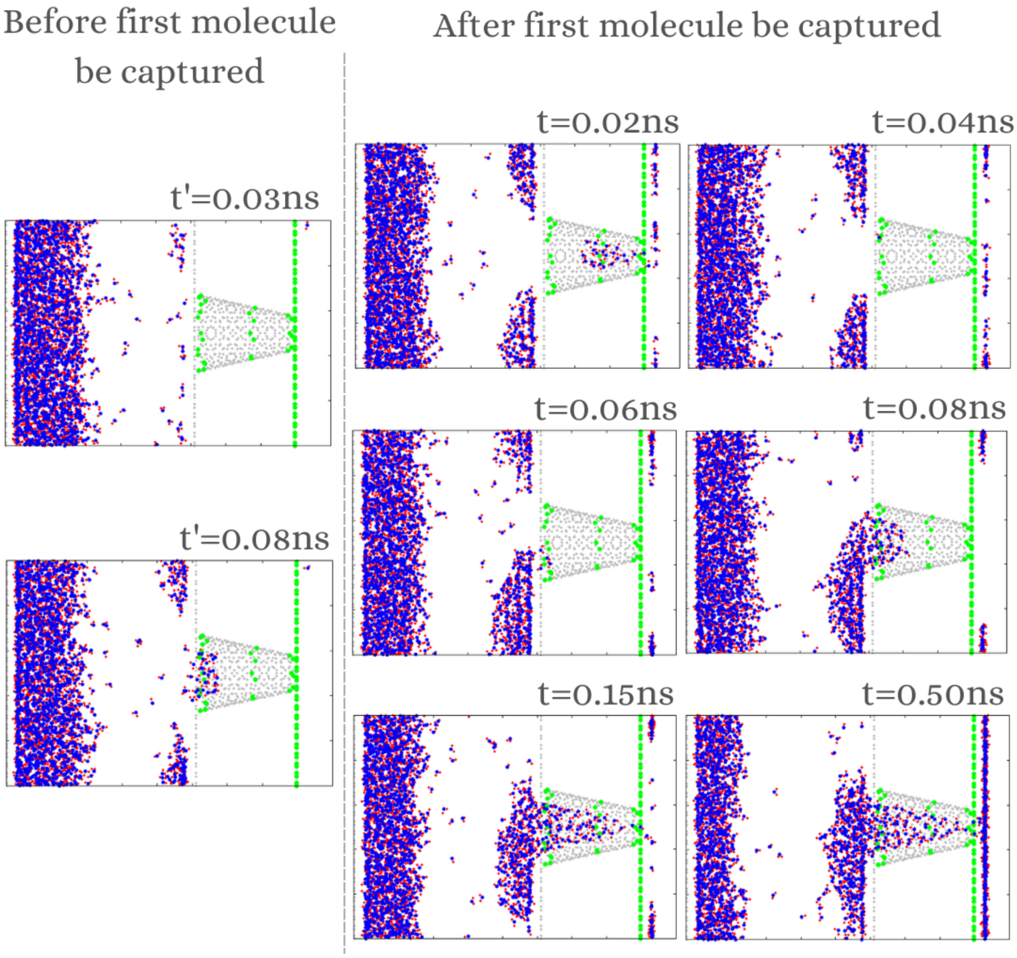

Figure 4: Snapshots of the temporal evolution for vapor system using $\epsilon_i = 1.1$.

drophilic sites of the nanocone as shown in Figure 4. Eventually, the droplets are moved from the middle and then to the tip of the nanocone due to the combination of hydrophilic and hydrophobic sites. Without them the droplet is stuck only at the base of the nanochannel. After an initial period (see $t = 0.15$ns in Figure 4), only a large droplet remains being absorbed by the nanocone, this drop is fed by the vapor forming a continuous flow of molecules that reach from the base to the tip of the nanocone, crossing to the collecting reservoir. This process stops once the collecting slab becomes full. The time it takes for this to happen, after first molecule be captured, depends on initial conditions, but it varies from $0.3 - 0.5$[ns].

The number of collected molecules and the histogram versus time for the vapor reservoir system are presented in Figure 5(a) and in Figure 5(b), respectively. Both graphs were obtained for one

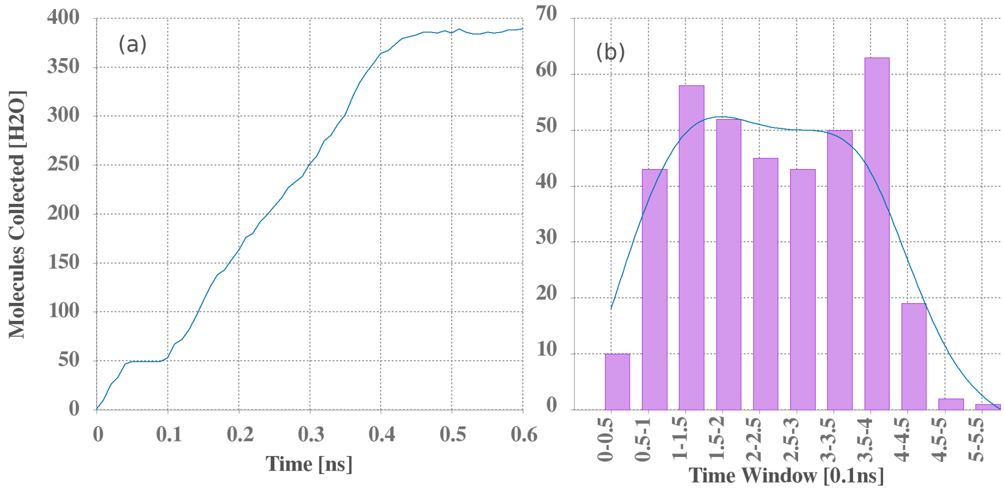

Figure 5: (a) Number and (b) Histogram of collected water molecules versus (a) time and (b) time intervals.

sample. The water harvesting (time interval $0.1 - 0.4$ ns) presents a linear growth, let's call it as Linear Regime. This regime is achieved when a large droplet is formed at the base of the nanocone, as described above, entering into the nanocone and forming a cohesive dynamics.

Figure 6 shows a snapshot of the water molecules on the hydrophilic slab of the collector reservoir, after the flow ceases and the number of water molecules in the reservoir becomes constant. Note that this molecules and its hydrogen bonds are arranged in a crystal-like arrangement. Figure 7 shows the radial distribution function, which is characteristics of an ordered structure in two dimensions. Figure 7(b) illustrates the mean square displacement of the water molecules on the collecting slab, indicating very small and constant mobility, confirming the ice-like behavior.

What does happen with the system when the water hydrophilic interactions with the surfaces are increased? In order to answer this question, Figure 8 illustrates the number of collected molecules versus time for different values of the water-wall attraction $\epsilon_r = 0.80, 0.95, 1.1, 1.3$ and 1.5. Each line is averaged over five samples. Note that the slopes of lines for fixed ϵ_r present a non monotonic behavior with ϵ_r. In order to understand the impact of varying attraction, we calculated the mean collected rate of molecules (MCR) per unit of time (10^{-2}ns) using

$$MCR = \sum_{i=0}^{i=t_{tot}} \frac{(Nm_i - Nm_{i-1})}{t_{tot}} \quad . \tag{1}$$

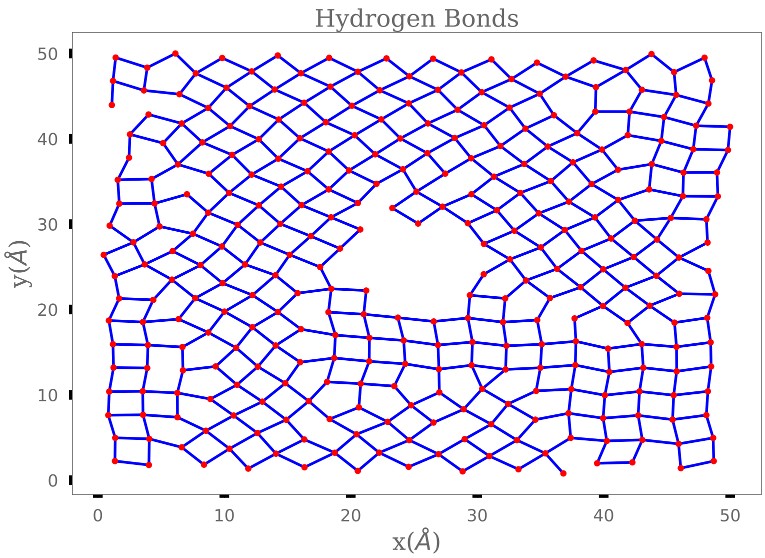

Figure 6: A snapshot of the water molecules (red points) on the attractive slab and hydrogen bonds (blue lines) in $t = 0.5$ns. The central region is where the nanocone is fitted, for this we did not plot the molecules on it. The hydrogen bonds where calculated using the distance and angles between water molecules.

Figure 8 (b) shows MCR of molecules versus ϵ_r. For values of ϵ_r below a certain threshold, the MCR increases with the increase of ϵ_r. The molecules movement in the nanocone depends on the combination of hydrophilic sites attracting and hydrophobic sites repulsion. Enhancing the hydrophilic attraction increases the number of water molecules attracted o the base of the nanocone. For values ϵ_r beyond a certain threshold, however, the MCR decreases. In this case, the rings are too attractive and water molecules tend to be stuck at the ring. The maximum rate occurs for $\epsilon_r \approx 1.1$.

In order to understand how ϵ_r impacts the water movement, we compute the flow. As a conical object diameter varies with length, so axial flux of molecules also varies from point to point in the cone. Therefore, we selected 10 regions equally spaced along the nanocone as shown in Figure 1 and we calculated the flux at each segment using the expression

$$J_i = \frac{n_{lrt} - n_{rlt}}{A_i N_{steps} \delta t} \tag{2}$$

where n_{lrt} is the number of molecules that cross a region of the nanontube from left to right, and

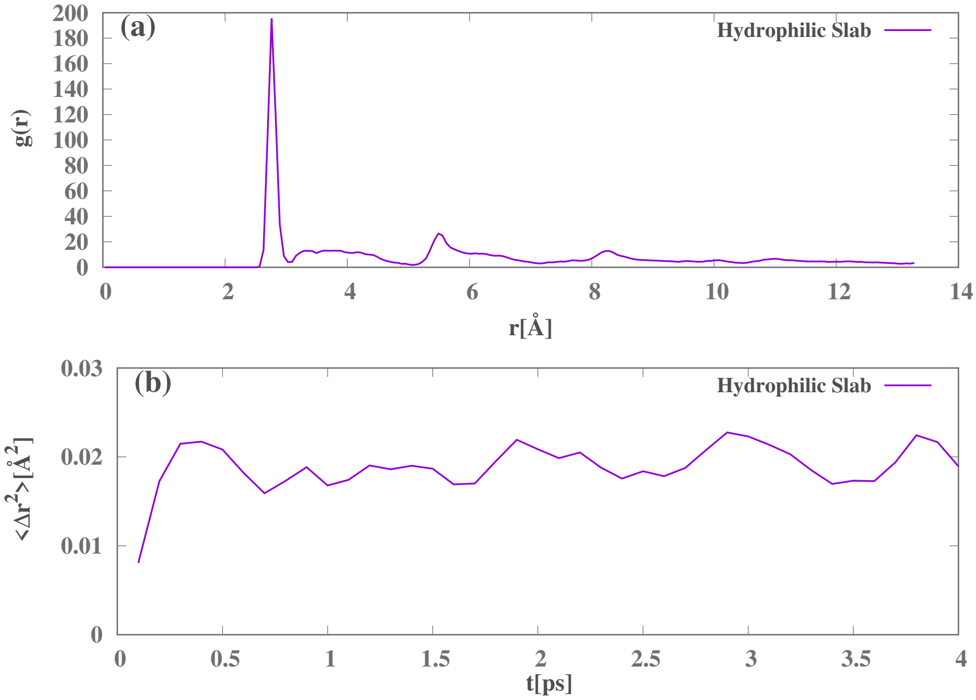

Figure 7: (a) The Radial Distribution Function and the (b) Mean Square Displacement of the water molecules on the attractive slab at $t = 0.5$ns and $\epsilon_r = 1.1$.

n_{rlt} from right to left. The $A_i = \pi a_{i,eff}^2$ is the area of the region i with radios a_i, and $a_{i,eff} = a_i - \sigma/2$ is the effective radius available for water $\sigma = 3.1589$. $N_{steps} = 10E4$ is the total number of steps used to calculate the flux, and $\delta t = 0.1$fs is the timestep.

Figure 9 shows the flux, J_i, as a function of the region (length) c_i (Figure 3) of the nanocone for different values of attraction ϵ_r. Each value was averaged over five samples with $8 \times 10E5$fs. This graph confirms the behavior observed in Figure 8 of the increase of water mobility with the increase of ϵ_r up to $\epsilon_r = 1.1$, and the decrease of J_i for $\epsilon_r > 1.1$. In addition Figure 9 shows the increase in J_i with the decrease of the diameter for the lower values of the hydrophobicity, $\epsilon_r = 0.80, 0.95, 1.1$.

For $\epsilon_r > 1.1$ a non monotonic behavior is observed. The decrease in flux with decreasing diameter for c_8, c_9, c_{10} and $\epsilon_r = 1.30, 1.50$ is a consequence of the high attraction of water molecules by the hydrophilic ring in the middle of the nanocone. The increase of the flux with the decrease of the radius is also observed with in carbon nanotubes [56]. The increase of flux followed by a decrease

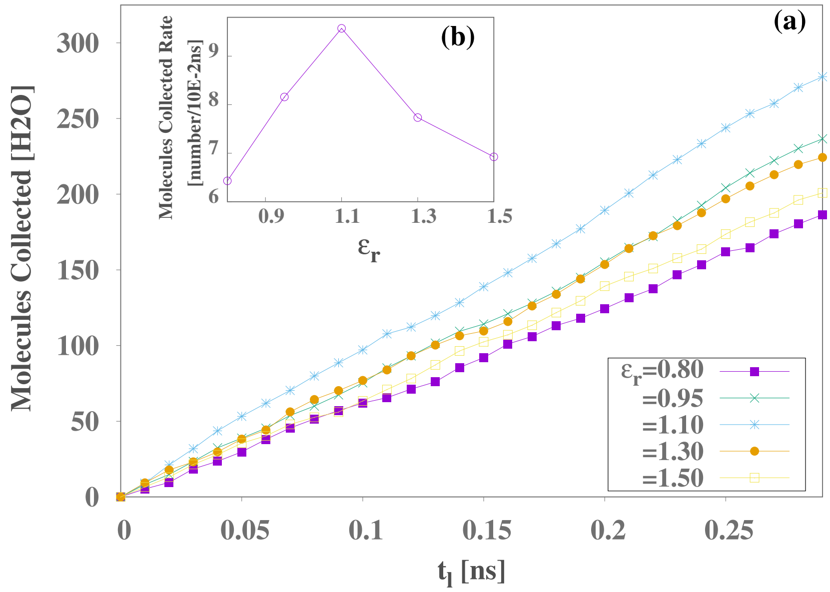

Figure 8: (a) Number of collected molecules versus time (ns) for different ϵ_r. (b) Mean collected rate (MCR) versus (ϵ_r).

with the increase of the hydrophobicity was also observed in transport properties of nanotubes with tunable hydrophilic sites [57,58].

Conclusions

Molecular dynamics simulations were conduced to study the water harvesting using the combination hydrophobic/hydrophilic sites on carbon nanocones in contact with a vapor water reservoir. The nanocone was constructed modeling three ring shaped hydrophilic regions. Differently from the simulations and experiments with water flow in nanotubes, no external pressure was applied. First, we observed that without the hydrophilic sites, no water enters the nanocone. Next, hydrophilic rings were introduced in the nanocone and different hydrophilic strength of the rings were explored.

The water dynamics is governed by the formation of droplets outside the nanocone and it presents a combination of regimes. First, droplets condense on the slab surface. Then, this droplets are attracted by the hydrophilic base of the nanocone, forming a larger drop, that enters into the cone

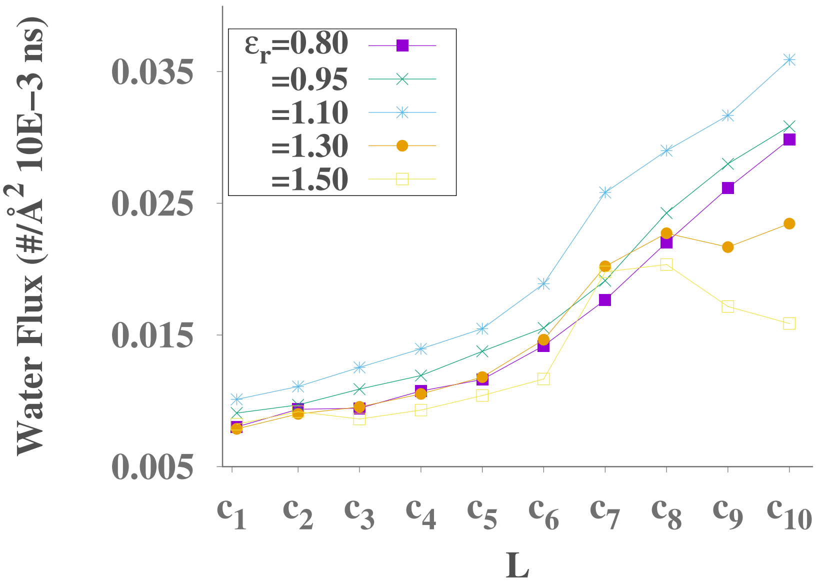

Figure 9: Graph of water flux in the different regions of the nanocone (Figure 3), for the different values of potential well ϵ_r.

generating a steady flux to the nanocone tip and reaching the collecting slab. This flow is generated by the combination of hydrophilic and hydrophobic sites.

The flow only stops once the collecting slab becomes full. The collecting slab is hydrophilic, attracting water molecules which becomes organized at the collecting slab surface. Water molecules on this slab form a very ordered structure, which freezes the water once the hydrophilic slab is completely filled. So the flow is interrupted even the collector being under thermostat with a temperature of 300k. An alternative to keep the flow of water would be to continuously remove water molecules from the collecting slab.

The strength ϵ_r of the hydrophilic sites affects the water collection and water mobility in two ways. Increasing ϵ_r pushes more droplets to the nanocone, but if ϵ_r is too large water molecules become trapped at the hydrophilic regions, decreasing water mobility.

Then, we can suggest the nanocone as an alternative to collect water from vapor without the use of high pressures if the nanocone would be a combination of hydrophobic and hydrophilic regions with an optimized ϵ_r.

Acknowledgements

The authors thank the computational infrastructure from CENAPAD/SP and CESUP/UFRGS.

Funding

This work was supported by the Brazilian agencies CNPq (through INCT-Fcx) and Coordenação de Aperfeiçoamento de Pessoal de Nível Superior (CAPES).

References

1. Mekonnen, M. M.; Hoekstra, A. Y. *Science Advances* **2016**, *2* (2), e1500323. doi:10.1126/sciadv.1500323.

2. Mapulanga, A. M.; Naito, H. *Proceedings of the National Academy of Sciences* **2019**, *116* (17), 8249–8254. doi:10.1073/pnas.1814970116.

3. Levia, D.; Creed, I.; Hannah, D. e. a. *Nature Geoscience* **2020**, *13*, 656–658. doi:10.1038/s41561-020-0641-y.

4. Ercin, A. E.; Hoekstra, A. Y. *Environment International* **2014**, *64*, 71–82. doi:https://doi.org/10.1016/j.envint.2013.11.019.

5. Ju, J.; Bai, H.; Zheng, Y.; Zhao, T.; Fang, R.; Jiang, L. *Nature Communications* **2012**, *3*, 1. doi:10.1038/alomms2253.

6. Köhler, M.; Bordin, J.; Barbosa, M. *The Journal of Chemical Physics* **2018**, *148*, 222804. doi:10.1063/1.5013926.

7. Abal, J. P. K.; Dillenburg, R. F.; Köhler, M. H.; Barbosa, M. C. *ACS Applied Nano Materials* **2021**, *4* (10), 10467–10476. doi:10.1021/acsanm.1c01982.

8. Zhou, X.; Lu, H.; Zhao, F.; Yu, G. *ACS Materials Letters* **2020**, *2* (7), 671–684. doi:10.1021/acsmaterialslett.0c00130.

9. Zhong, L.; Zhu, L.; Li, J.; Pei, W.; Chen, H.; Wang, S.; Razaa, A.; Khan, A.; Hou, Y.; Zheng, Y. *Mol. Syst. Des. Eng.* **2021**, *6*, 986–996. doi:10.1039/D1ME00019E.

10. Wahlgren, R. V. *Water Research* **2001**, *35* (1), 1–22. doi:https://doi.org/10.1016/S0043-1354(00)00247-5.

11. Wang, J.; Liu, J.; Wang, R.; Wang, L. *Applied Thermal Engineering* **2017**, *127*, 1608–1616. doi:https://doi.org/10.1016/j.applthermaleng.2017.09.063.

12. Ura, D. P.; Knapczyk-Korczak, J.; Szewczyk, P. K.; Sroczyk, E. A.; Busolo, T.; Marzec, M. M.; Bernasik, A.; Kar-Narayan, S.; Stachewicz, U. *ACS Nano* **2021**, *15* (5), 8848–8859. doi:10.1021/acsnano.1c01437. PMID: 33900735

13. LaPotin, A.; Kim, H.; Rao, S. R.; Wang, E. N. *Accounts of Chemical Research* **2019**, *52* (6), 1588–1597. doi:10.1021/acs.accounts.9b00062. PMID: 31090396

14. Mohd, G.; Majid, K.; Lone, S. *ACS Applied Materials & Interfaces* **0**, *0* (0), null. doi:10.1021/acsami.1c20463. PMID: 34985254

15. Vega, C.; Abascal, J. L. F. *Phys. Chem. Chem. Phys.* **2011**, *13*, 19663–19688. doi:10.1039/C1CP22168J.

16. Zheng, Y.; Bai, H.; Huang, Z.; Tian, X.; Nie, F.-Q.; Zhao, Y.; Zhai, J.; Jiang, L. *Nature* **2010**, *463*, 640–3. doi:10.1038/nature08729.

17. Parker, A.; Lawrence, C. *Nature* **2001**, *414*, 33–4. doi:10.1038/35102108.

18. Bai, H.; Zhang, C.; Long, Z.; Geng, H.; Ba, T.; Fan, Y.; Yu, C.; Li, K.; Cao, M.; Jiang, L. *J. Mater. Chem. A* **2018**, *6*, 20966–20972. doi:10.1039/C8TA08267G.

19. Dai, X.; Sun, N.; Nielsen, S. O.; Stogin, B. B.; Wang, J.; Yang, S.; Wong, T.-S. *Science Advances* **2018**, *4* (3), eaaq0919. doi:10.1126/sciadv.aaq0919.

20. Wang, X.; Zeng, J.; Yu, X.; Liang, C.; Zhang, Y. *Applied Surface Science* **2019**, *465*, 986–994. doi:https://doi.org/10.1016/j.apsusc.2018.09.210.

21. Cao, M.; Xiao, J.; Yu, C.; Li, K.; Jiang, L. *Small* **2015**, *11* (34), 4379–4384. doi:https://doi.org/10.1002/smll.201500647.

22. Kell, G. S. *J. Chem. Eng. Data* **1967**, *12*, 66–69. doi:10.1021/acs.chemrev.5b00611.

23. Angell, C. A.; Finch, E. D.; Bach, J. *J. Chem. Phys.* **1976**, *65*, 3065.

24. Netz, P. A.; Starr, F. W.; Stanley, H. E.; Barbosa, M. C. *J. Chem. Phys.* **2001**, *115*, 344.

25. Corti, H. R.; Appignanesi, G. A.; Barbosa, M. C.; Bordin, J. R.; Calero, C.; Camisasca, G.; Elola, M. D.; Franzese, G.; Gallo, P.; Hassanali, A.; Huang, D. L.; C., M.; Montes de Oca, J. M.; Longinotti, M. P.; Rodriguez, J.; Rovere, M.; Scherlis, D.; Szleifer, I. *European Physical Journal E* **2021**, *44*, 1–50. doi:https://doi.org/10.1140/epje/s10189-021-00136-4.

26. Holt, J. K.; Park, H. G.; Wang, Y.; Stadermann, M.; Artyukhin, A. B.; Grigoropoulos, C. P.; Noy, A.; Bakajin, O. *Science* **2006**, *312* (5776), 1034–1037. doi:10.1126/science.1126298.

27. Köhler, M. H.; Bordin, J. R.; de Matos, C. F.; Barbosa, M. C. *Chemical Engineering Science* **2019**, *203*, 54–67. doi:https://doi.org/10.1016/j.ces.2019.03.062.

28. Barati Farimani, A.; Aluru, N. R. *The Journal of Physical Chemistry B* **2011**, *115* (42), 12145–12149. doi:10.1021/jp205877b. PMID: 21913716

29. Köhler, M. H.; Bordin, J. R.; da Silva, L. B.; Barbosa, M. C. *Physica A: Statistical Mechanics and its Applications* **2018**, *490*, 331–337. doi:https://doi.org/10.1016/j.physa.2017.08.030.

30. Bordin, J. R.; Barbosa, M. C. *Physica A: Statistical Mechanics and its Applications* **2017**, *467*, 137–147. doi:https://doi.org/10.1016/j.physa.2016.10.007.

31. Hong, Y.; Zhang, J.; Zhu, C.; Zeng, X. C.; Francisco, J. S. *Journal Material Chemistry A* **2019**, *7*, 3583–3591. doi:https://doi.org/10.1039/C8TA10941A.

32. Zhou, Z.; Gao, T.; McCarthy, S.; Kozbial, A.; Tan, S.; Pekker, D.; Li, L.; Leu, P. W. *Carbon* **2019**, *152*, 474–481. doi:https://doi.org/10.1016/j.carbon.2019.06.012.

33. Ozden, S.; Ge, L.; Narayanan, T. N.; Hart, A. H. C.; Yang, H.; Sridhar, S.; Vajtai, R.; Ajayan, P. M. *ACS Applied Materials & Interfaces* **2014**, *6* (13), 10608–10613. doi:10.1021/am5022717. PMID: 24896731

34. Karousis, N.; Suarez-Martinez, I.; Ewels, C. P.; Tagmatarchis, N. *Chemical Reviews* **2016**, *116* (8), 4850–4883. doi:10.1021/acs.chemrev.5b00611. PMID: 27074223

35. Schaub, T. A. *Angewandte Chemie International Edition* **2020**, *59* (12), 4620–4622. doi:https://doi.org/10.1002/anie.201914830.

36. Voiry, D.; Pagona, G.; Canto, E. D.; Ortolani, L.; Morandi, V.; Noé, L.; Monthioux, M.; Tagmatarchis, N.; Penicaud, A. *Chem. Commun.* **2015**, *51*, 5017–5019. doi:10.1039/C4CC10389K.

37. Hassan, J.; Diamantopoulos, G.; Homouz, D.; Papavassiliou, G. *Nanotechnology Reviews* **2016**, *5*, . doi:10.1515/ntrev-2015-0048.

38. Curcio, M.; Cirillo, G.; Saletta, F.; Michniewicz, F.; Nicoletta, F. P.; Vittorio, O.; Hampel, S.; Iemma, F. *C* **2020**, *7* (1), 3. doi:10.3390/c7010003.

39. Li, W.; Wang, W.; Zheng, X.; Dong, Z.; Yan, Y.; Zhang, J. *Computational Materials Science* **2017**, *136*, 60–66. doi:https://doi.org/10.1016/j.commatsci.2017.04.024.

40. Sarapat, N., P.and Thamwattana; Cox, B. J.; Baowan, D. *Journal of Mathematical Chemistry* **2020**, *58*, 1650–1662.

41. Li, W.; Wang, W.; Hou, Q.; Yan, Y.; Dai, C.; Zhang, J. *Journal of hysical Chemistry Letters* **2017**, *8*, 435–439.

42. Li, W.; Wang, W.; Hou, Q.; Yan, Y.; Dai, C.; Zhang, J. *Physical Chemistry Chemical Physics* **2018**, *20*, 27910.

43. Li, W.; Wang, W.; Zhang, Y.; Yan, Y.; Dai, C.; Kral, P.; Zhang, P. K. J. *Carbon* **2018**, *129*, 374–379. doi:https://doi.org/10.1016/j.carbon.2017.12.039.

44. Razmkhah, M.; Mosavian, M.; Moosavi, F. *Desalination* **2017**, *407*, 103–115. doi:10.1016/j.desal.2016.12.019.

45. Chandra, A.; Keblinski, P. *The Journal of Chemical Physics* **2020**, *153* (12), 124505. doi:10.1063/5.0018726.

46. Rokoni, A.; Sun, Y. *The Journal of Chemical Physics* **2020**, *153* (14), 144706. doi:10.1063/5.0024722.

47. Krishnan, A.; Dujardin, E.; Treacy, M. M. J.; Hugdahl, J.; Lynum, S.; Ebbesen, T. W. *Nature* **1997**, *388* (6641), 451–454. doi:10.1038/41284.

48. Karousis, N.; Suarez-Martinez, I.; Ewels, C. P.; Tagmatarchis, N. *Chemical Reviews* **2016**, *116* (8), 4850–4883. doi:10.1021/acs.chemrev.5b00611. PMID: 27074223

49. Plimpton, S. *Journal of Computational Physics* **1995**, *117* (1), 1–19. doi:https://doi.org/10.1006/jcph.1995.1039.

50. Abascal, J. L. F.; Vega, C. *The Journal of Chemical Physics* **2005**, *123* (23), 234505. doi:10.1063/1.2121687.

51. Tsimpanogiannis, I.; Moultos, O.; Mercier Franco, L. F.; Spera, M.; Erdos, M.; Economou, I. *Molecular Simulation* **2018**, *45*, 1–29. doi:10.1080/08927022.2018.1511903.

52. Vega, C.; de Miguel, E. *The Journal of Chemical Physics* **2007**, *126* (15), 154707. doi:10.1063/1.2715577.

53. Alejandre, J.; Chapela, G. A. *The Journal of Chemical Physics* **2010**, *132* (1), 014701. doi:10.1063/1.3279128.

54. Vins, Václav,; Celný, David,; Planková, Barbora,; Nemec, Tomás,; Duska, Michal,; Hrubý, Jan, *EPJ Web of Conferences* **2016**, *114*, 02136. doi:10.1051/epjconf/201611402136.

55. Losey, J.; Kannam, S. K.; Todd, B. D.; Sadus, R. J. *The Journal of Chemical Physics* **2019**, *150* (19), 194501. doi:10.1063/1.5086054.

56. Qin, X.; Yuan, Q.; Zhao, Y.; Xie, S.; Liu, Z. *Nano Letters* **2011**, *11*, 2173–2177. doi:https://doi.org/10.1021/nl200843g.

57. Moskowitz, I.; Snyder, M. A.; Mittal, J. *The Journal of Chemical Physics* **2014**, *141* (18), 18C532. doi:10.1063/1.4897974.

58. Melillo, M.; Zhu, F.; Snyder, M. A.; Mittal, J. *The Journal of Physical Chemistry Letters* **2011**, *2* (23), 2978–2983. doi:10.1021/jz2012319. PMID: 25606067